International Journal of Pharmaceutics: X 3 (2021) 100090

Contents lists available at ScienceDirect

International Journal of Pharmaceutics: X

journal homepage: www.sciencedirect.com/journal/international-journal-of-pharmaceutics-x

The use of X-ray microtomography to investigate the microstructure of pharmaceutical tablets: Potentials and comparison to common physical methods

Ann Kathrin Schomberg [a,b,1,*], Alexander Diener [a,1], Isabell Wünsch [a,b], Jan Henrik Finke [a,b], Arno Kwade [a,b]

[a] Technische Universität Braunschweig, Institute for Particle Technology, Volkmaroder Straße 5, 38104 Braunschweig, Germany
[b] Technische Universität Braunschweig, Center of Pharmaceutical Engineering (PVZ), Franz-Liszt-Straße 35A, 38106 Braunschweig, Germany

ARTICLE INFO

Keywords:
X-ray microtomography
Tablet microstructure
API homogeneity
Micro-cracks
Pore size distribution
Tablets

ABSTRACT

Within this study, tablets microstructure was investigated by X-ray microtomgraphy. The aim was to gain information about their microstructure, and thus, derive deeper interpretation of tablet properties (mechanical strength, component distribution) and qualified property functions. Challenges in image processing are discussed for the correct identification of solids and voids. Furthermore, XMT measurements are critically compared with complementary physical methods for characterizing active pharmaceutical ingredient (API) content and porosity and its distribution (mercury porosimetry, calculated tablet porosity, Focused Ion Beam-Scanning Electron Microscopy (FIB-SEM)). The derived porosity by XMT is generally lower than the calculated porosity based on geometrical data due to the resolution of the XMT in relation to the pore sizes in tablets. With rising compactions stress and API concentration, deviations between the actual and the calculated API decrease. XMT showed that API clusters are present for all tablets containing >1 wt% of ibuprofen. The 3D orientation of the components is assessable by deriving cord lengths along all dimensions of the tablets. An increasing compaction stress leads to rising cord lengths, showing higher connectivity of the respective material. Its lesser extent in the z-direction illustrates the anisotropy of the compaction process. Additionally, cracks in the fabric are identified in tablets without visible macroscopic damage. Finally, the application of XMT provides valuable structural insights if its limitations are taken into account and its strengths are fostered by advanced pre- and post-processing.

1. Introduction

Tableting is an important production process in various industries, such as the food, chemical and pharmaceutical industry. The prediction of mechanical and application-oriented tablet properties, e.g. tensile strength and active pharmaceutical ingredient (API) distribution, based on raw material properties and process parameters is still very difficult and hardly possible. Therefore, the formulation and process development is still mainly empirical. The mechanical and application-oriented tablet properties are primarily determined by the microstructure of the tablet, which is in turn affected by various material, formulation and process parameters, such as particle size and shape, deformation behavior, composition of the powder mixture and compaction stress (Hiestand et al., 1977; Leuenberger et al., 1989; Juppo, 1996; Wünsch et al., 2021; Alderborn et al., 1985; Nordström et al., 2013; Sun, 2017). The lack of comprehension regarding the process-structure-property-relationship is certainly one of the main reasons for the absent predictability of tablet properties. For that reason, a systematic investigation of the influence of material and process parameters on the microstructure of tablets is required. In this case, the microstructure is addressed by the density, pore size distribution, and the distribution of the components of a formulation within the tablet framework. Different studies show the suitability of the non-destructive X-ray microtomography (XMT) for the 3D characterization of particulate structures and especially of solid dosage forms (Feinauer et al., 2015; Strege et al., 2014; Leißner et al., 2020; Busignies et al., 2006; Sinka et al., 2004; Landis and Keane, 2010; Gioumouxouzis et al., 2020; Hancock and Mullarney, 2005; Maire and Withers, 2014). First studies of the

* Corresponding author at: Technische Universität Braunschweig, Institute for Particle Technology, Volkmaroder Straße 5, 38104 Braunschweig, Germany.
E-mail address: a.schomberg@tu-braunschweig.de (A.K. Schomberg).
[1] These authors contributed equally.

https://doi.org/10.1016/j.ijpx.2021.100090
Received 6 July 2021; Accepted 7 July 2021
Available online 10 July 2021

suitability of XMT for the characterization of the microstructure of compacted materials were performed by Lannutti (Lannutti, 1997) and by Burch (Burch, 2002). Both studies investigated the density distribution inside compacted ceramic. This is also the focus of different studies in the pharmaceutical area. Several studies like Sinka et al., Wray et al. and Busignies et al. investigated the density distribution inside pharmaceutical tablets (Sinka et al., 2004; Wray et al., 2008; Busignies et al., 2006; Akseli et al., 2011), while other investigations consider the density distribution inside ribbons produced by roller compaction (Akseli et al., 2011; Miguélez-Morán et al., 2009; Wiedey and Kleinebudde, 2017; Sun et al., 2018). Another focus of XMT measurements is the investigation of microcracks inside tablets and the correlation of the findings with the occurrence of tablet defects, (e.g. capping and lamination), as well as tablet tensile strength (Hancock and Mullarney, 2005; Garner et al., 2014; Yost et al., 2019; Mazel et al., 2018; Ma et al., 2020; Wu et al., 2008). Besides normal tablets, bilayer tablets were investigated to determine the impact of local density distributions on the delamination of the two layers (Akseli et al., 2013; Inman et al., 2007). Additionally, investigations of the porosity and pore structure inside primary particles (Fang et al., 2017), granules (Farber et al., 2003; Crean et al., 2010) and tablets (Markl et al., 2017; Markl et al., 2018) were performed. Beyond structural analyses, drug release processes were investigated with XMT (Li et al., 2012). However, these investigations were limited by the resolution of XMT, which is typically above 0.5 µm for high resolution XMT (Strege et al., 2014). In contrast to that, mercury intrusion porosity (MIP) measurements of pharmaceutical tablets indicate pore sizes smaller than this resolution, so that the depiction of all existing pores by XMT is not possible (Sun, 2017; Markl et al., 2017). This could be one reason for the limited number of investigations, which studied the distribution of the single components of a formulation, especially of the API, inside pharmaceutical tablets. Rigby et al. showed the inhomogeneous distribution of the API amiodarone inside controlled release tablets (Rigby et al., 2004). The drug particle distribution in mini-tablets containing moxidectin was investigated by Wagner-Hattler et al. using synchrotron XMT (Wagner-Hattler et al., 2020). The authors found a non-uniform distribution of the API, indicating a particle movement to the outer boundaries of the tablet during compression. Neumann et al. (Neumann et al., 2019) examined the excipient, API and pore distribution on pharmaceutical tablets, consisting of ibuprofen and microcrystalline cellulose, using synchrotron tomography and introduced a novel method for image trinarization. However, the tablets must be cut into small pieces and the pores filled with a contrast medium for the analysis. Thus, the microstructure could be affected by the mechanical cutting or swelling effects caused by the contrast medium. The examined cubic volumes size was $(0.3\ mm)^3$ which allowed a detailed analysis of the pore structure. The investigation of formulation and process parameters on the API distribution is limited. Bollmann et al. investigated the pre-processing step by applying different methods for different tablet batches, concluding that one processing procedure is not applicable for all binary mixtures investigated (Bollmann and Kleinebudde, 2021).

In this study, a systematical investigation of the microstructure of tablets compressed at different compaction stresses and with varying ibuprofen content was conducted using XMT. The objective consists of resolving the microstructure and linking it to macroscopic mechanical properties of the tablets to better understand effects such as decreasing tensile strength as well as the homogeneity of oral solid dosage forms. Therefore, a trade-off between the resolution and the scanned region of interest was necessary. In the following, the approaches to identify and characterize the pore network as well as API distribution inside tablets using XMT are introduced and their possibilities and limitations are discussed.

2. Materials and methods

2.1. Materials

The pharmaceutical excipient microcrystalline cellulose (MCC, x_{10} = 20 µm, x_{50} = 63 µm, x_{90} = 139 µm, Vivapur® 101, JRS Pharma, Rosenberg, Germany) and the active pharmaceutical ingredient ibuprofen (IBU, x_{10} = 9 µm, x_{50} = 31 µm, x_{90} = 34 µm Novartis Pharma, Basel, Switzerland) were selected as materials. MCC mainly consists of elongated primary particles and of approximately spherical agglomerates, while the particle shape of IBU is approximately rectangular (Fig. 1). The solid density determined by helium pycnometry is 1.544 g/cm^3 for MCC and 1.112 g/cm^3 for IBU. Additionally, magnesium stearate (Faci, Carasco GE, Italy) was used as lubricant.

2.2. Methods

2.2.1. Powder characterization

Particle size analysis was performed using the laser light diffraction instrument HELOS in combination with the dry dispersion unit RODOS for MCC and the wet dispersion unit SUCELL (all: Sympatec, GmbH, Clausthal-Zellerfeld, Germany) for IBU. IBU was dispersed in deionized water and the dispersion aid Polysorbat 20 was added. The particle shape of the powders was characterized by scanning electron microscopy (SEM) using the device LEO 1550 (Carl Zeiss, Oberkochen, Germany)(Fig. 1). The particles were spread on carbon pads and sputter-coated with gold. The solid densities of the powders were determined by helium pycnometry using the device ULTRAPYC 1200e (Quantachrome Instruments, Boynton Beach, FL, USA). Double measurements with 10 measurement points each were performed and the mean values were calculated.

2.2.2. Preparation of binary mixtures

Binary mixtures of MCC and IBU with varying IBU concentration (1, 5, 15, 25 and 50 wt%) were prepared using a Turbula® mixer (Willy A. Bachofen, Muttenz, Switzerland) with a rotational speed of 49 rpm. The volume of the mixing container was 1 L and was filled up to 60% with the powders. The mixing time was set to 15 min. Before mixing, IBU was sieved (mesh size: 1 mm) for the destruction of large agglomerates.

2.2.3. Tableting

The binary mixtures were compacted using the compaction simulator Styl'One Evolution (MEDEL'PHARM, Beynost, France). The simulator was operated using the compression profile of a camshaft with a maximum punch velocity of 20 mm/s and was equipped with flat-faced, round punches with a diameter of 11.28 mm. The die was manually lubricated with magnesium stearate and 450 mg of the respective mixture was manually filled into the die. Two test series were performed: one under variation of the compaction stress (50, 75, 100, 150 and 200 MPa) using the mixture with an IBU concentration of 50 wt % and one under variation of the IBU concentration (1, 5, 15, 25 and 50 wt%) at a constant compaction stress of 200 MPa.

2.2.4. Tablet characterization

The tablets were stored under constant ambient conditions of 25 + − 2 °C and 45 + − 15% r.H. for at least 24 h. As these humidity values are maximum possible fluctuations guaranteed and, moreover, the tablets have been stored in containers, the actual humidity range relevant for the tablets was much smaller. Afterwards, the weight of the tablets was measured and tablet height, diameter and breakage force were characterized for 10 tablets using the tablet tester MultiTest 50 FT (Sotax AG (Dr. Schleuniger), Aesch, Switzerland). The mass and the geometrical dimensions were used for the calculation of the tablet porosity ε_T as follows:

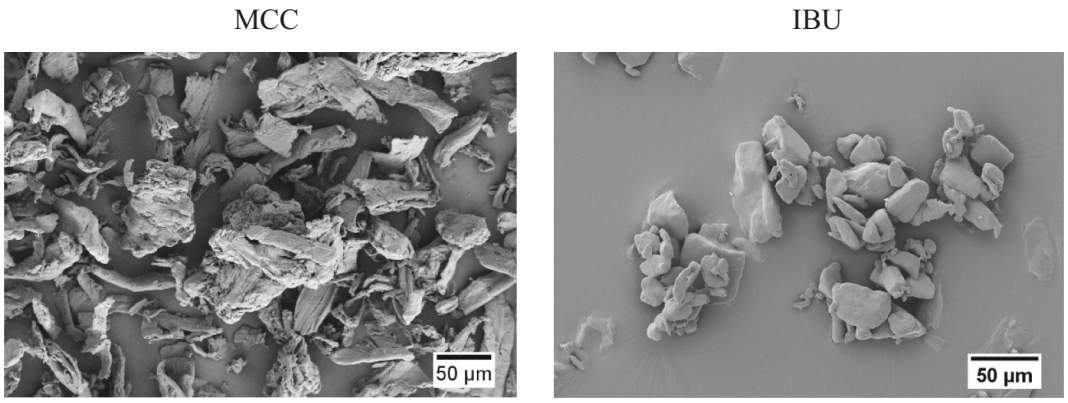

Fig. 1. SEM images of the MCC and IBU powders.

$$\varepsilon_T = 1 - \frac{\rho_T}{\rho_s} = 1 - \frac{4 \bullet m_T}{\pi \bullet d_T^2 \bullet} h_T \bullet \rho_s \quad (1)$$

where ρ_T is the tablet density, ρs is the calculated solid density of the respective powder mixture, m_T is the tablet mass, d_T is the tablet diameter and h_T is the tablet height. Additionally, the tablet tensile strength was calculated using the diametral breakage force F (Fell and Newton, 1970):

$$\sigma_t = \frac{2 \bullet F}{\pi \bullet d_T \bullet h_T} \quad (2)$$

The IBU concentration of the tablets used for the investigation with XMT (one tablet per process parameter setting) was controlled using UV-VIS spectroscopy. Each tablet was dissolved in 0.1 M sodium hydroxide solution and the supernatant was filtered before analysis. The absorption of the solution was measured using the UV-VIS spectrometer SPECORD 210 Plus (Analytik Jena, Jena, Germany) at a wave length of 264 nm. The IBU concentration was calculated based on the Lambert-Beer's law, considering a previously established calibration curve. Furthermore, the pore size distribution of the tablets containing 50 wt% IBU and compacted at 100 MPa and 200 MPa was exemplarily determined by Mercury Intrusion Porosimetry (MIP) using the device PoreMaster® 60 (Quantachrome Instruments, Boynton Beach, FL, USA). The penetrometer was filled with two tablets per sample. Low pressure (up to 0.344 MPa) and high pressure operations (up to 414 MPa) were performed and the pore size distributions were calculated based on the Washburn Eq. (Washburn, 1921). For an optical evaluation of the inner tablet porosity, dual focused ion beam in combination with scanning electron microscopy (FIB-SEM, Helios G4 CX, FEI Company, USA) was used. The pixel size of the SEM image was 10.4 nm, the image was taken by 10 kV source voltage and 0.2 nA current.

2.2.5. X-ray microtomography

The high resolution X-ray microtomograph (XMT) MicroXCT-400 (Zeiss (Xradia), Germany) was used for the microstructural examination of the tablets. The voxel size depends on the volume of the scanned region of interest (ROI) and on the sample size. The XMT measuring settings (Table 1) were chosen by considering the trade-off between a large ROI for a representative analysis volume and a small voxel size to generate detailed structural information. The pixel size is 5.06 µm for all experiments and was chosen according to the settings so that the microstructure over the complete height of the tablet could be investigated. The chosen magnification resulted in a measuring time of approximately 1.5 h. One tablet was characterized per compaction stress and IBU concentration.

Table 1
Micro XCT-400 settings.

Source	Detector
Voltage: 40 kV Current: 200 µA Power: 8 W	Objective: 4 X Camera Binning: 2 Exposure time: 1.5 s

Each investigated tablet was positioned on the rotation stage and was exposed to an X-ray beam emitted by the X-ray source. Hence, the volume of interest was measured concentric to the axial axis of the tablet (Fig. 2). A scintillator converts the transmitted X-ray beam into visible light, which is magnified by an objective and is used for the generation of a projection image on a CDD detector. One projection image was taken for each rotation step. Overall, 3000 projection images were taken and reconstructed to a stack of 2D cross-sectional images using the software XMReconstructur (Zeiss (Xradia), Oberkochen, Germany).

2.2.6. Image processing

Image processing is a crucial step for the characterization of microstructural properties and was performed for the improvement and quantification of the 3D image. After the reconstruction, the grayscale images were filtered, an analysis volume V_A was extracted and segmented into the three phases MCC, IBU and pore volume (Fig. 3).

A non-local-mean filter algorithm was used, included in the software Avizo Fire (Thermo Fisher Scientific Inc., Waltham, MA, USA) for the reduction of noise and the improvement of the contrast. Further image processing was performed using Matlab (MathWorks, Natick, MA, USA). The analysis volume VA was extracted to save computational time and to exclude measuring artifacts along the border region (Fig. 5). Before the extracted volume V_A was used for further analysis, it had to be ensured that the volume is high enough to be representative, e.g. regarding phase volume fraction, of course assuming a homogeneous distribution of the phases. Thus, a representative elementary volume (REV) analysis was performed to determine the minimum volume at which the volume fraction of IBU φ_{Ibu} is not linked to the volume V_A any more (Sun et al., 2018). For this purpose, the volume fraction of IBU φ_{Ibu} in the solid phase was examined for the tablet with 50 wt% IBU compressed at 200 MPa in a cuboid-shaped analysis volume with an increasing side length L_{ext} from 0.0506 mm up to 2.53 mm (Fig. 4). Here, the volume fraction of IBU is approximately constant for an analysis volume above $(0.75\ mm)^3$, representing a REV. The analysis volume V_A should be at least of the same size as the REV to generate valid results. Regarding the aim to gain as much information of the inner tablet structure as possible, the horizontal projection area of the extracted analysis volume V_A was set to $(2.53\ mm)^2$ multiplied by the tablet height for all experiments. The tablet height differed between 4.2 and 3.7 mm, depending on the applied compaction stress of 50 to 200 MPa. Thus, the extracted analysis volume V_A is high enough to generate valid results. A 3D image and a top view of the representative proportions in contrast to the tablet volume and the scanned volume are presented (Fig. 5 a, b).

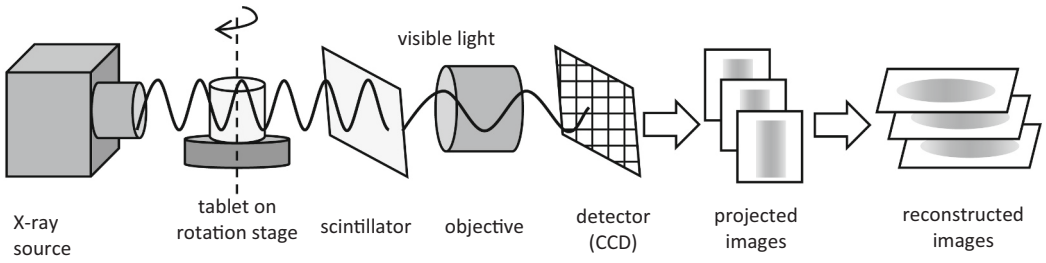

Fig. 2. Schematic representation of the XMT principle (adapted from (Landis and Keane, 2010)).

Fig. 3. Schematic representation of image processing.

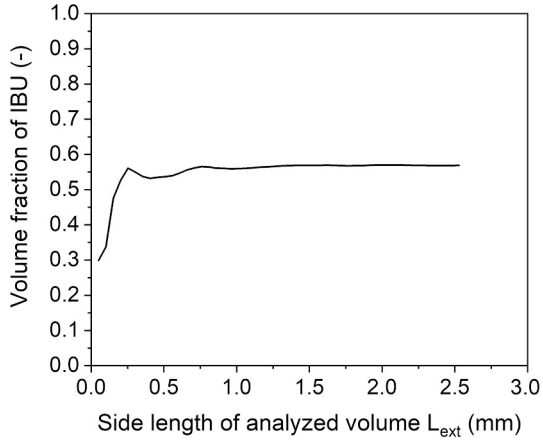

Fig. 4. Determination of REV for volume fraction of ibuprofen in the solid fraction for the tablet compressed at 200 MPa.

2.2.7. *Image segmentation*

For the detailed analysis of the tablet microstructure, especially for the calculation of the volume fractions of MCC, IBU and pores, an image segmentation is necessary. Image segmentation is performed by analyzing the frequency distribution of the grayscale pixel intensity (image histogram) and dividing it into three different phases by defining thresholds. For the segmentation between the solid and the void phase, a manually set threshold was applied in a way that only all clearly visible and identifiable pores were taken into account. Segmentation of IBU and MCC was done using the automated segmentation algorithm by Otsu, which is implemented in the Matlab function "multithresh" (Otsu, 1979). Otsu was used as it is a simple and robust algorithm, which enables the segmentation of different phases.

For the investigation of the pore diameter distribution from the XMT images, the pore network was segmented into single pores by using the watershed method applied by the software Avizo Fire. Subsequently, the separated pores were detected and the pore volume as well as the frequency distribution of the pore volume q_3 were calculated. Based on the pore volumes, the diameters were calculated, assuming only spherical pores.

In order to gain information about the connectivity, anisotropy and accumulation of the solid phases, the cord length was investigated with GeoDict 2019 (Math2Market GmbH, Kaiserslautern, Germany). It was calculated for each of the three dimensions separately, by summing up the successive voxels of the respective phase. The result is a cord length distribution (Torquato and Lu, 1993).

2.2.8. *Derivation of porosity and solid volume concentration*

The porosity ε_{XMT}, yielded from XMT measurements and image processing, is derived by calculating the ratio of the sum of the volume elements (voxels) belonging to the void phase ν_{void} (x,y,z) to the total number of voxels inside the analyzed domain location ν (x,y,z) (Eq. 3), where x, y and z describe the three dimensions.

$$\varepsilon_{XMT} = \frac{\sum \nu_{void}(x,y,z)}{\sum \nu_{void}(x,y,z) + \sum \nu_{MCC}(x,y,z) + \sum \nu_{IBU}(x,y,z)} \tag{3}$$

The volume concentrations $\varphi_{XMT,i}$ of the solid phases MCC and IBU in the XMT images are calculated by the ratio of the sum of voxels belonging to the respective solid phase ν_i (x,y,z) to the total number of voxels representing the solid phase inside the analyzed domain location

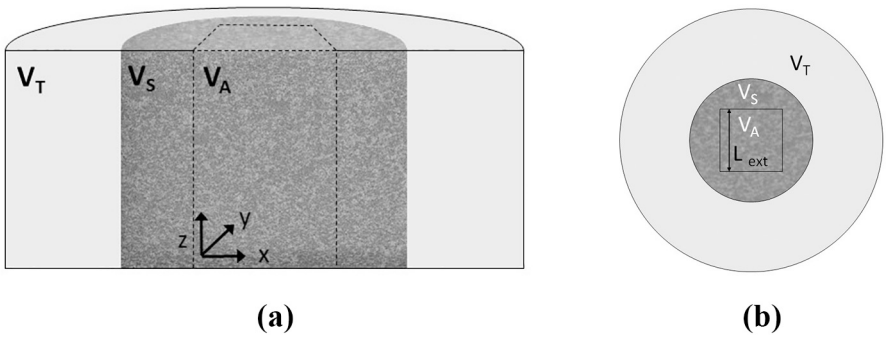

Fig. 5. Schematic representation of the proportions of the tablet volume V_T, the scanned volume V_S and the extracted analysis volume V_A in (a) a 3D presentation of a cross section and (b) a top view.

ν (x,y,z) (Eq. 4).

$$\varphi_{XMT,i} = \frac{\sum v_i(x,y,z)}{\sum v_{MCC}(x,y,z) + \sum v_{IBU}(x,y,z)} \quad (4)$$

The theoretical volume concentration $\varphi_{theo,i}$ is calculated based on the solid density ρ_i and the mass concentration $c_{m,i}$ of the respective solid phase i (Eq. 5). The obtained values are then compared to the results of the solid volume concentration, provided by XMT, $\varphi_{XMT,i}$.

$$\varphi_{theo,i} = \frac{\frac{c_{m,i}}{\rho_i}}{\sum_{j=1}^{J}\left(\frac{c_{m,j}}{\rho_j}\right)} \quad (5)$$

2.2.9. Calculation of the homogeneity

For the investigation of the distribution of IBU inside the tablets, and thus, for the evaluation of the homogeneity, V_A was divided into 360 cuboid volume elements, six in x and y direction, respectively, and ten in z direction (Fig. 6). The side length of each volume element was selected to be about 2.5 times larger than the particle size x_{90} of MCC, representing the particle size at which 90% of MCC particles are smaller than the specified value. The side length in z-direction is related to the tablet height and is therefore a function of the compaction stress (side length of a cube in z-direction: 360 to 410 µm). Afterwards, the homogeneity of the IBU distribution was calculated using the empirical normalized standard deviation σ_h, considering the concentration of IBU in each volume element i, $\varphi_{XMT,IBU}$(i), as well as the concentration of IBU in the analysis volume V_A of the respective tablet, $\varphi_{XMT,IBU}(V_A)$ (Eq. 6).

$$\sigma_h = \frac{1}{\varphi_{XMT,IBU}(V_A)}\sqrt{\frac{1}{n-1}\sum_{i=1}^{n}\left(\varphi_{XMT,IBU}(i) - \varphi_{XMT,IBU}(V_A)\right)2} \quad (6)$$

3. Results and discussion

In the following, the results of the segmentation are critically discussed by comparing them to volume fractions obtained by other methods. Subsequently, the microstructure, provided by XMT, is presented. Here, API clusters and cracks inside the tablet can be observed. Furthermore, the pore network for the tablets is investigated by means of a pore size distribution and the connectivity of the material in x-, y- and z-direction is displayed using the cord length.

3.1. Evaluation of image processing and segmentation strategies

3.1.1. Evaluation of porosity segmentation

The porosity ε_{XMT} (Eq. 3), yielded from the segmented 3D images, is compared to the tablet porosity ε_T calculated by using the geometrical dimensions of the tablets (Eq. 1). Both methods show a comparable progress (Fig. 7 a), while ε_{XMT} is considerably lower with 9.2% and 4.6% at 50 MPa and 200 MPa, respectively. At low compaction stresses of 50 and 75 MPa, about 50% of the calculated porosity is identifiable by XMT and the subsequent image processing, while the ratio decreases to about 22% at 200 MPa.

The apparent pore size distribution of the tablets has a considerable impact on the segmentation results. Due to the given resolution of 5.06 µm, only a certain quantity of the void phase could be detected by XMT examination. However, the similar course of the curve confirms an appropriate segmentation, so it can be assumed that the difference is mainly affected by the limited resolution.

For a deeper investigation of the pore size distribution, MIP measurements of tablets compacted at 100 and 200 MPa were carried out (Fig. 8a). In addition, SEM images of a FIB cut of a tablet compacted at 200 MPa were produced (Fig. 8b). In fact, MIP results present a considerably high proportion of pores with diameters lower than 3 µm and 1 µm for the tablets compressed at 100 MPa and 200 MPa, respectively. However, the total pore volume corresponds to the out-die data (Fig. 7). The pore size distribution is shifted to smaller sizes with increasing compaction stress, as expected. Regarding the resolution of the XMT images of 5.06 µm (dashed line in diagram Fig. 8 a), 96.2% of the pores are smaller than the voxel size for 100 MPa as well as 80% for 200 MPa and, therefore, are not detectable. However, it has to be considered that the calculation of the pore size distribution is based on the Washburn-equation assuming cylindrical pores. The intruded mercury volume at a given pressure is assigned to the inlet diameter of the pore, which is filled with mercury at this pressure. Therefore, MIP rather yields a pore bottleneck distribution because the volume of the subsequent, most likely coarser pores are attributed to the characteristic diameter of the certain bottleneck (Schüth, 2002). It is most likely that bottlenecks especially occur on the tablet surface, where mostly very small pore sizes result as a function of high local stresses due to the confinement of the punches and the die. Accordingly, the mercury must pass these pores to enter the tablet pore network. Moreover, MIP is not able to detect closed pores within the tablet structure.

The SEM image confirms that pores with a diameter lower than the voxel size of 5.06 µm are present. However, a considerably coarser void space is observable on the left side of the image, which indicates that there are pores with diameters above 5.06 µm. Therefore, these pores are detectable in the XMT images, representing between 50% and 22% of the geometrically estimated porosity for the 50 MPa and 200 MPa tablets, respectively. Thus, the used XMT method is valid to show lager pores (> 5.06 µm) as well as the overall decrease of the porosity. Furthermore, the geometric diameter of all pores within the tablet volume can be assessed without the restriction that bottlenecks are taken as

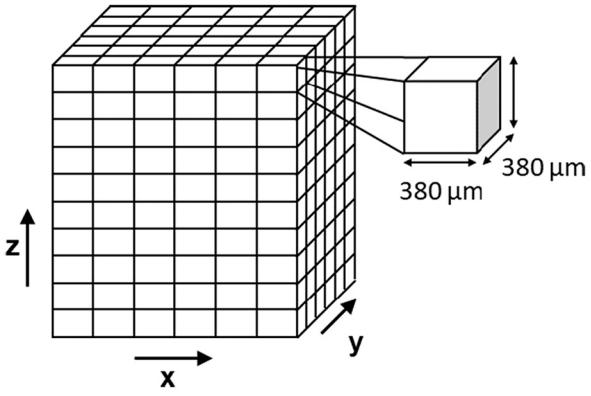

Fig. 6. Schematic representation of the division of V_A into rectangular volume elements for the evaluation of the homogeneity of the IBU distribution.

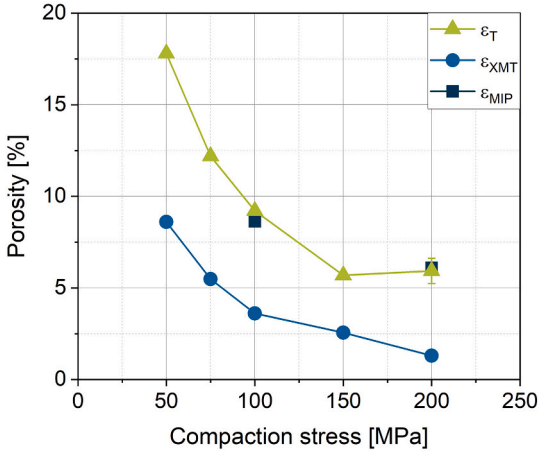

Fig. 7. Comparison of porosity determined by geometrical dimensions ε_T, by XMT ε_{XMT} and by MIP ε_{MIP}.

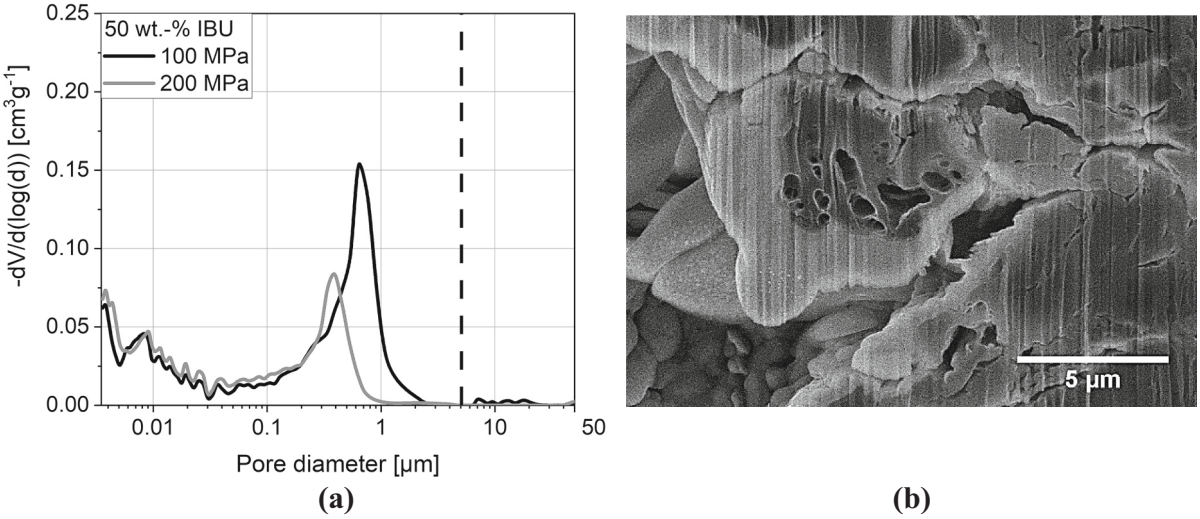

Fig. 8. Pore size distribution determined by MIP (a), the dashed line marks the voxel side length of 5.06 µm and SEM image of a FIB cut close to the tablet surface of a tablet containing 50 wt% IBU compressed at 200 MPa (b).

representative values for all pore sizes in a chain of pores.

The tablet porosity is only characterized by XMT for the tablets with an IBU concentration of 50 wt% at different compaction stresses. For the images with varying IBU concentration, the contrast between void phase and IBU was too low. This can be traced back to the application of the maximum compression stress (200 MPa) for the production of these tablets and hence, to the low tablet porosities ε_T (Table 2) and pore sizes. Therefore, only the solid phases (MCC and IBU) are segmented. Accordingly, for the tablets with a IBU concentration up to 25 wt%, a considerably high void volume is expected to be wrongly assigned to the solid phases during segmentation. Regarding the tablet compressed at 50 MPa with 50 wt% IBU, where only about half (8.6%) of the porosity (17.8%) is detected, the error for this tablet is comparable to the error of the tablets with different IBU content, since also about 10% void space is not taken into account.

3.1.2. *Results of the segmentation for the solid components*

Besides the identification of the pores, the differentiation of the solid phase between MCC and IBU is a challenge as well. As for the porosity, the correct estimation of the volume concentrations of each solid component is an indication of the quality of the image segmentation. In order to classify whether the investigation by XMT and the subsequent segmentation process provide reliable information about the concentration of the solid content, the solid volume concentrations of MCC and of IBU determined using the segmented 3D images are compared to values determined by theoretical assumptions and by UV-VIS spectrometry. To enable the direct comparison of the data obtained by UV-VIS with the XMT data, the investigation was always done for exactly the same tablet as used for the XMT examination. However, the UV-VIS measurement assessed the concentration in the whole tablet while the XMT only assessed the central cylinder of V_A (see Fig. 4).

The theoretical volume fractions φ_{theo} of MCC and IBU, calculated based on the aspired blend composition (Eq. 5), are constant for the varied compaction stresses due to the same IBU concentration. The volume fractions calculated from UV-VIS measurements $\varphi_{UV\text{-}VIS}$ are in very good accordance with the theoretical fractions for the tablets compressed at 50 and 75 MPa (Fig. 9 a). Tablets compressed at 100, 150 and 200 MPa show slightly lower IBU concentrations than expected which most likely results from variation of IBU concentration inside the powder blend. Furthermore, the volume fractions of IBU obtained by XMT are about 5% higher than for UV-VIS for the tablets compressed at 50, 75 and 100 MPa. At 150 MPa, a slightly lower difference between the values is observable. In fact, for 200 MPa, there is good agreement between all three methods, although the XMT-measured porosity is approx. 78% lower than the calculated porosity based on the geometry (Fig. 7). However, the porosity after this compression stress is generally low at 5.93% for the geometrically derived porosity.

When considering that $\varphi_{XMT,MCC}$ and $\varphi_{XMT,IBU}$ should have a constant relation of the solid volume concentration independent of the applied stress, the deviation can be understood as a result of wrongly segmented or not detected void phases. Consequently, a wrongly segmented or not detected void phase is assigned to one or both solid phases. While $\varphi_{XMT,IBU}$ is overestimated, $\varphi_{XMT,MCC}$ is underestimated, suggesting that a part of the pore volume is wrongly segmented as IBU. This hypothesis is supported by the fact that IBU has a lower solid density compared to MCC. Therefore, IBU generally displays lower intensities (represented by darker gray values in the unprocessed XMT images) than MCC, while a void phase possesses the lowest intensity (shown in black). In the case of pores, which are smaller than the resolution of 5.06 µm and located inside IBU, the voxels show a medium intensity still well differentiable form voids. Thus, these voxels are most likely segmented as IBU and, due to the presence of air in the assigned voxels, the resulting volume fraction of IBU is even higher than it should be. If the pores are located inside MCC, i.e. inter-particulate and intra-particulate porosity, and represent a considerably high proportion of the respective voxel volume, the mean density within such voxels is medium and result in medium intensity as well. As an example, a voxel containing approx. 27% voids and 73% MCC possesses the same apparent density and consequently, the same intensity as pure, solid IBU and is segmented as IBU accordingly. Therefore, these voxels are also segmented as IBU. Only in the case, that the pores inside the MCC have a low ratio to the voxels volume, they fall under the distribution of intensities, which are assumed to be MCC. Summing up these cases, there is a significant proportion of pores which might wrongly be segmented as IBU. This challenge can be solved by using a higher resolution. Subsequently, the scanned region decreases in size, which makes the analysis and subsequent conclusions referred to the microstructure of the whole tablet difficult.

With increasing compaction stress, the porosity decreases, and thus

Table 2
Geometrically calculated porosity of the tablets compressed at 200 MPa.

IBU mass concentration (wt%)	1	5	15	25	50
Corresponding IBU volume concentration (vol%)	1.38	7.41	15.95	31.35	56.74
Porosity ε_T (%)	10.14	9.83	9.03	8.89	5.93

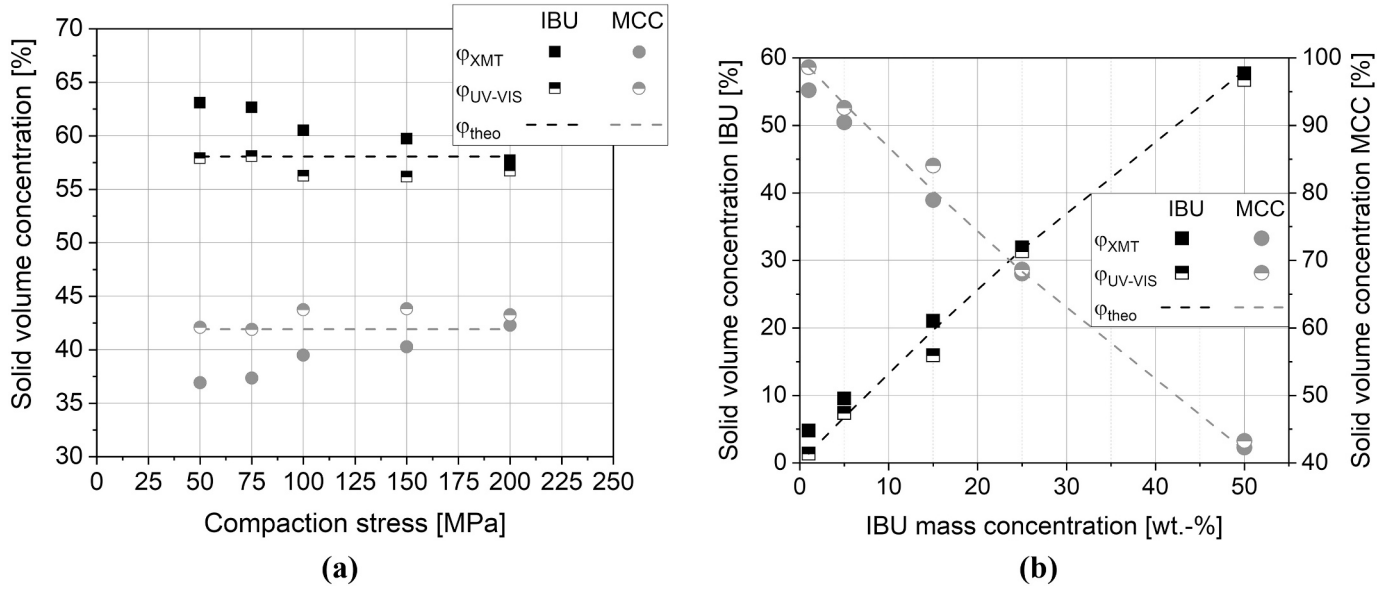

Fig. 9. Comparison of volume fraction within the solid phases of 50 wt% IBU tablets (a) and tablets with varying IBU concentration compacted at 200 MPa (b), determined by XMT, UV-VIS and the theoretical volume fraction calculated by eq. 4.

the difference between ε_{geo} and ε_{XMT} also decreases, resulting in lower volume fractions which are wrongly assigned to the solid phases. Therefore, the difference between φ_{XMT} and $\varphi_{UV-V_{IS}}$ decreases as well (Fig. 10 a). As the porosity decreases, the number of voxels which are erroneously assigned to the solid phase declines. Simultaneously, the pore size decreases, as shown by MIP, which both results in apparent densities closer to the respective solid density. This leads to an easier and therefore higher quality of segmentation of the solid phases, as seen for the tablet compressed at 200 MPa with an IBU concentration of 50 wt%.

For the tablets with varying IBU concentration, the volume fractions measured by UV–Vis $\varphi_{UV\text{-}VIS}$ are in good accordance to the theoretical solid volume fractions φ_{theo}, except for 15 wt% (Fig. 9 b). In the 3D images, obtained by XMT, the volume fraction of IBU is again higher compared to the other two methods. With increasing IBU content, the overestimation of the IBU concentration decreases from about 4% to about 1%, until the volume fractions are in good accordance for 25 and 50 wt% (Fig. 10 b). However, the resulting deviations are lower than expected regarding the high porosity of about 10%, which is not segmented as such, but assigned to the solid phases. This could be explained by small pore sizes, which arises from the high compaction stress of 200 MPa. Therefore, a considerably high ratio of the pores is expected to be below the resolution of 5.06 µm. As described, small pores inside the MCC particles or neighboring particles are segmented as MCC, if the proportion of the void phase in the voxel in question is low enough (< 27 vol%). Otherwise the voxel is segmented as IBU, leading to the higher deviation at low IBU concentrations. The geometrically determined porosity ε_T decreases with increasing IBU concentration. Simultaneously, a rising share of the void phase is located inside or on adjoining particles of IBU and are accordingly segmented as IBU. As a result, the distribution of the solid volume fraction is closer to the one measured by UV–Vis.

However, results for φ_{UV-VIS} and φ_{theo} are based on the examination of whole tablets while φ_{XMT} relates to an analysis volume of $(2.53\ mm)^2$ multiplied by the tablet height taken from the middle of the tablet. Therefore, the measured values by UV-VIS may not necessarily match the exact same values yielded by XMT – especially if IBU is not

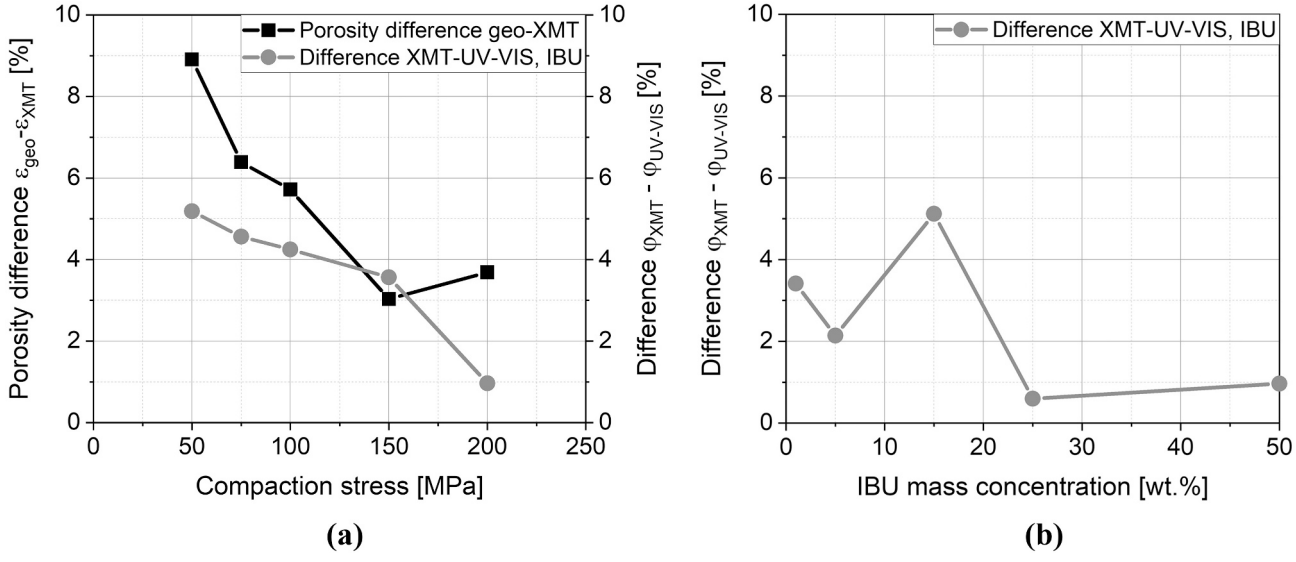

Fig. 10. Porosity difference compared with difference in solid phase concentrations derived from XMT and UV–Vis.

homogeneously distributed inside the tablet or due to the density distribution from the center to the edge in flat-faced tablets (Cabiscol et al., 2018).

3.2. Structural evaluation of the microstructure in XMT images

In order to get a general impression of the microstructure obtained by XMT, segmented images for the variation of the compaction stress as well as for the variation of the IBU content were studied (Fig. 11). The images are 2D vertical cuts through the 3D analysis volume, and thus, just provide a local impression. In both instances, large clusters of IBU are observable.

For the images with varying IBU content, clusters were observed at IBU mass concentrations of 5 wt% and above. With increasing IBU concentration, the number of clusters tends to rise. However, the identification of the clusters is more difficult for higher IBU concentrations (i.e. 50 wt%) as higher contact areas between neighboring clusters of IBU are developed. The clusters of IBU are most probably results of the powder preparation and insufficient blending process. IBU was sieved with a mesh size of 1 mm, thus agglomerates with slightly lower sizes entered the blending process. Due to the low kinetic and shear energy which is induced by the turbula mixer as well as to the high cohesivity of IBU, the agglomerates were only slightly dispersed and may reagglomerate. Therefore, they remained in the blend, which was filled into the dies, and they are found in the segmented images of the tablets – even for low IBU contents. Furthermore, the IBU clusters in the tablets are anisometric with larger dimensions in the horizontal direction and, by that, perpendicular to the vertically exerted stress of compaction. This hints at the preferential orientation of the clusters during the filling of the die, the higher compression of such clusters along the main vertical stress axis, or a combination of both. The length of connected voxels of the same phase and its orientation is discussed in section 3.6.

Besides the IBU distribution, the pores can be observed in the cutouts of the images of the variation of the compaction stress (Fig. 10, left). With increasing compaction stress, the size as well as the number of pores identified by segmentation in the images decrease, as expected.

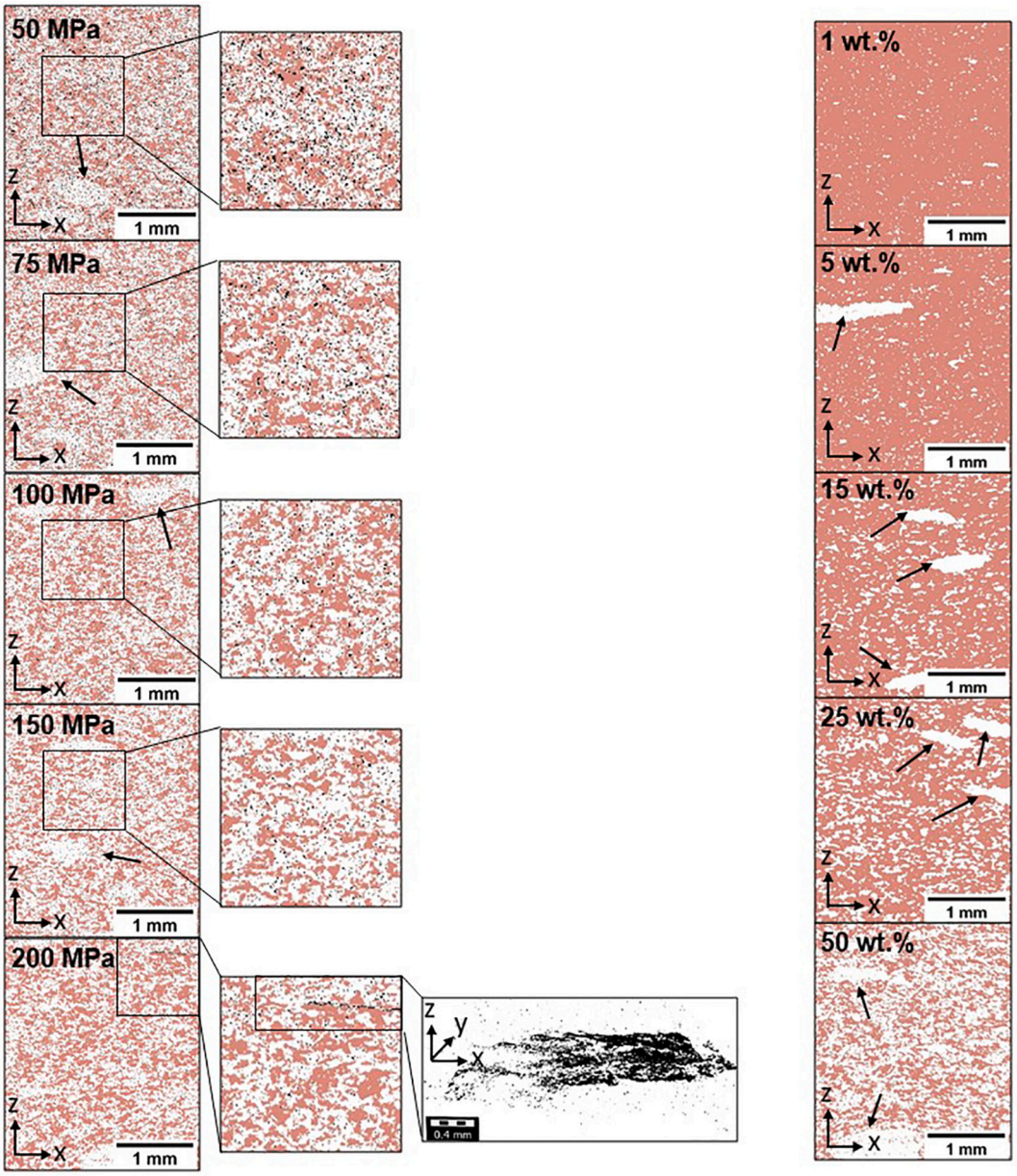

Fig. 11. Segmented images of a vertical cut (x-z plane) for: tablets containing 50 wt% IBU compacted at various compaction stresses (left) with cut-out magnifications (2nd from left) and tablets with varying IBU content compacted at 200 MPa (right).

For the tablet compacted at 200 MPa, horizontal cracks can be observed. Both, the large IBU clusters as well as the observed cracks will be addressed further in the following.

Black arrows highlight IBU clusters. Black pixels correspond to pores, white to IBU and red to excipient (MCC). Depiction of only the pores for the tablet compacted at 200 MPa in a 3D image indicates the occurrence of a horizontal crack (3rd from left).

3.3. Homogeneity of IBU distribution

XMT enables the localized analysis of the homogeneity within the tablet itself. This is of special interest as considerable IBU clusters were observed for weight fractions of 5 wt% up to 50 wt% (Fig. 11). Accordingly, the distribution of IBU is examined following the method described in section 2.2.9 to evaluate the homogeneity. The variation of the compaction stress shows no clear influence on the IBU distribution at 50 wt% (Fig. 12 a), as expected. The results for σ_h fluctuate between 5% and 10%, showing no dependency of the compaction stress, but indicating a non-uniform IBU distribution on the micro scale.

For the variation of the IBU mass concentration, there is a high discrepancy between the σ-values for 1 wt% and 5 wt% (Fig. 12 b) due to the occurrence of large IBU clusters for the latter (compare Fig. 11). As the overall concentration of IBU increases, the empirical normalized standard deviation becomes smaller due to the higher IBU concentration in each volume element. Thus, the difference between the IBU content in volume elements with clusters compared to the overall content decreases. This dependency of the variation coefficient on the IBU content is in accordance with literature describing the blending process in general (Venables and Wells, 2001). The results indicate that the inhomogeneous distribution of IBU is mainly a result of the mixing and the filling process of the die. Therefore, these sub-processes should be carefully designed and implemented to achieve the desired IBU homogeneity in the tablets.

3.4. Pore size distribution

Considering the amount of porosity detected with XMT, a detailed pore size distribution including the small pores cannot reasonably be described with the resolution used. Nevertheless, the pore size distribution of the detected pores can be determined. The analysis of the pore network helps understanding the mechanical properties of the tablets as well as linking them to the microstructure. Hence, the pore network is separated into single pores using the watershed method. The volume of the separated voids is calculated which is afterwards used to calculate the diameter of a volume equivalent sphere to describe the pore diameter. A volume frequency distribution – as commonly used for the description of particle size distributions – is used to present the pore size distribution (Fig. 13). The tablet compressed at 50 MPa shows high pore diameters and almost no small pores, which can be related to the challenge to separate the relatively coarse pores correctly. At low compression stresses, the porosity is high, so the pores are well cross-linked and have comparatively large bottlenecks between the individual cavities. For the application of the watershed algorithm, this is a challenge to distinguish the individual pores, resulting in clusters of pores which are defined to be one pore. The not precise separation of the pores leads to the high proportion of large void volume for 50 MPa. With rising compression stress up to 150 MPa, the maximum pore diameter decreases, while the proportion of small pores rises significantly, as expected. In contrast, the tablet compressed at 200 MPa presents a high proportion of large pores, which are about the same size as for 50 MPa. They correspond to the cracks in the tablet found in the segmented images (Fig. 11). As MIP detects most pores with a pore diameter considerably smaller than 5 µm, it is not useful to compare the two distributions.

3.5. Tablet defects

The systematic variation of the compaction stress for an IBU concentration of 50 wt% present tablet defects depending on the compaction stress. For the tablet compressed at 200 MPa and an IBU content of

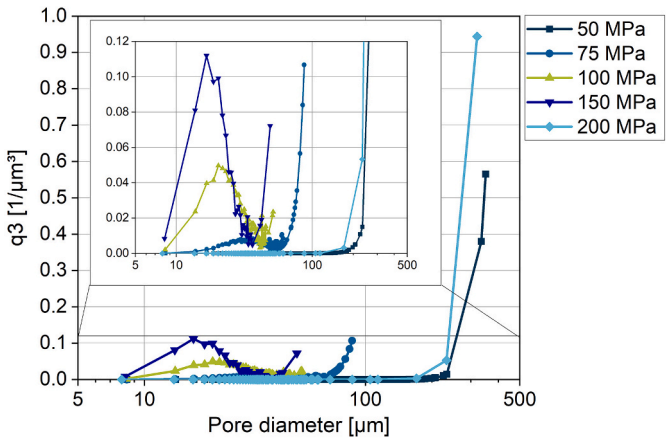

Fig. 13. Volume frequency distribution of pores determined by XMT, applying watershed method, over the pore diameter.

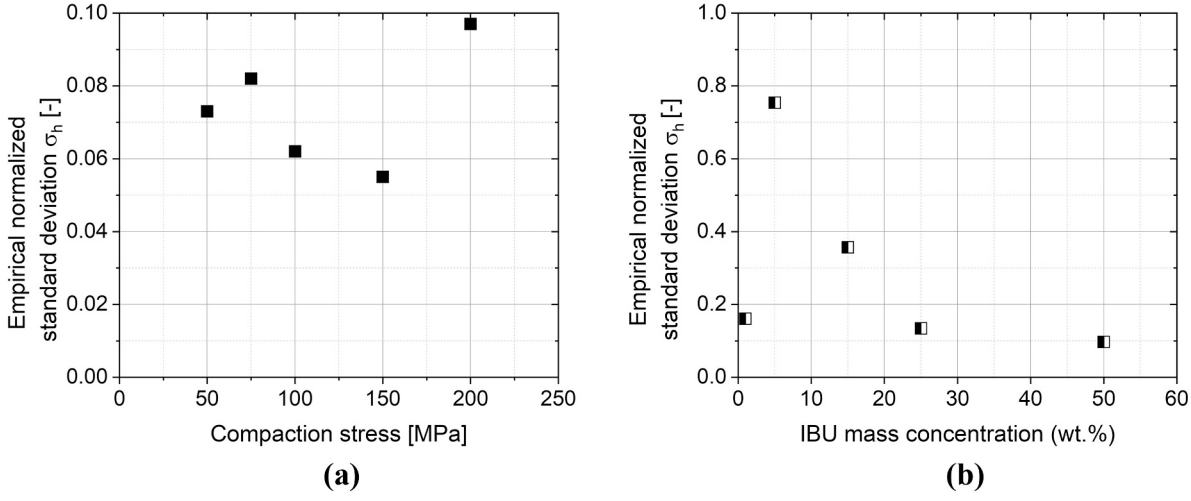

Fig. 12. Homogeneity of IBU distribution (a) in relation to compaction stress for 50 wt% of IBU and (b) in relation to weight fraction of IBU compacted at 200 MPa.

50 wt%, defects in form of horizontal cracks are observed (Fig. 14 c and 14 d). In contrast, the 3D visualization of the porosity distribution for the tablet compressed at 150 MPa shows, as expected, a higher porosity compared to 200 MPa but no cracks are observable (Fig. 14 a and b). In addition, the tensile strength for the tablets compressed at 200 MPa decreases considerably (Fig. 15 a). The lower strength results from the microstructure, which is weakened by the crack. As ten tablets are investigated to examine the strength, cracks seem to occur for several tablets with the same formulation compacted at 200 MPa. These findings can be related to an increased instantaneous elastic recovery at the maximum applied compaction stress for tablets of pure IBU ($n = 5$) (Fig. 15 b). In contrast, the instantaneous elastic recovery for MCC, as well as for the formulation with 50 wt% IBU, is considerably lower. Thus, MCC dominates the behavior concerning the instantaneous elastic recovery for the blend. Therefore, it is hypothesized that large clusters of IBU lead to high local stresses due to the differing instantaneous elastic recovery of MCC and IBU, as it is not able to expand significantly to reduce the elastically stored energy. Thus, the high local mechanical relaxation stress in normal direction may result in the occurrence of cracks, as the local contact strength of the neighboring particles for IBU as well as for MCC is exceeded. For the tablets with lower IBU content up to 25 wt%, no cracks are observed in the images. In addition, although a decreasing trend in tensile strength can be seen with increasing IBU content, there is no sudden drop and no significantly higher standard deviation below 50 wt% (Fig. 15 c). Therefore, up to a certain IBU concentration, MCC seems to be able to build a linked microstructure, which compensates the recovery energy of IBU.

Cracks inside tablets were also found by Wu et al. using XMT measurements to investigate capping on lactose tablets (Wu et al., 2008; Wu et al., 2005; Wu et al., 2007). The cracks found in these studies, however, display different local orientation with diagonal cracks as compared to cracks parallel to the punch surfaces in our case (Fig. 14 d).

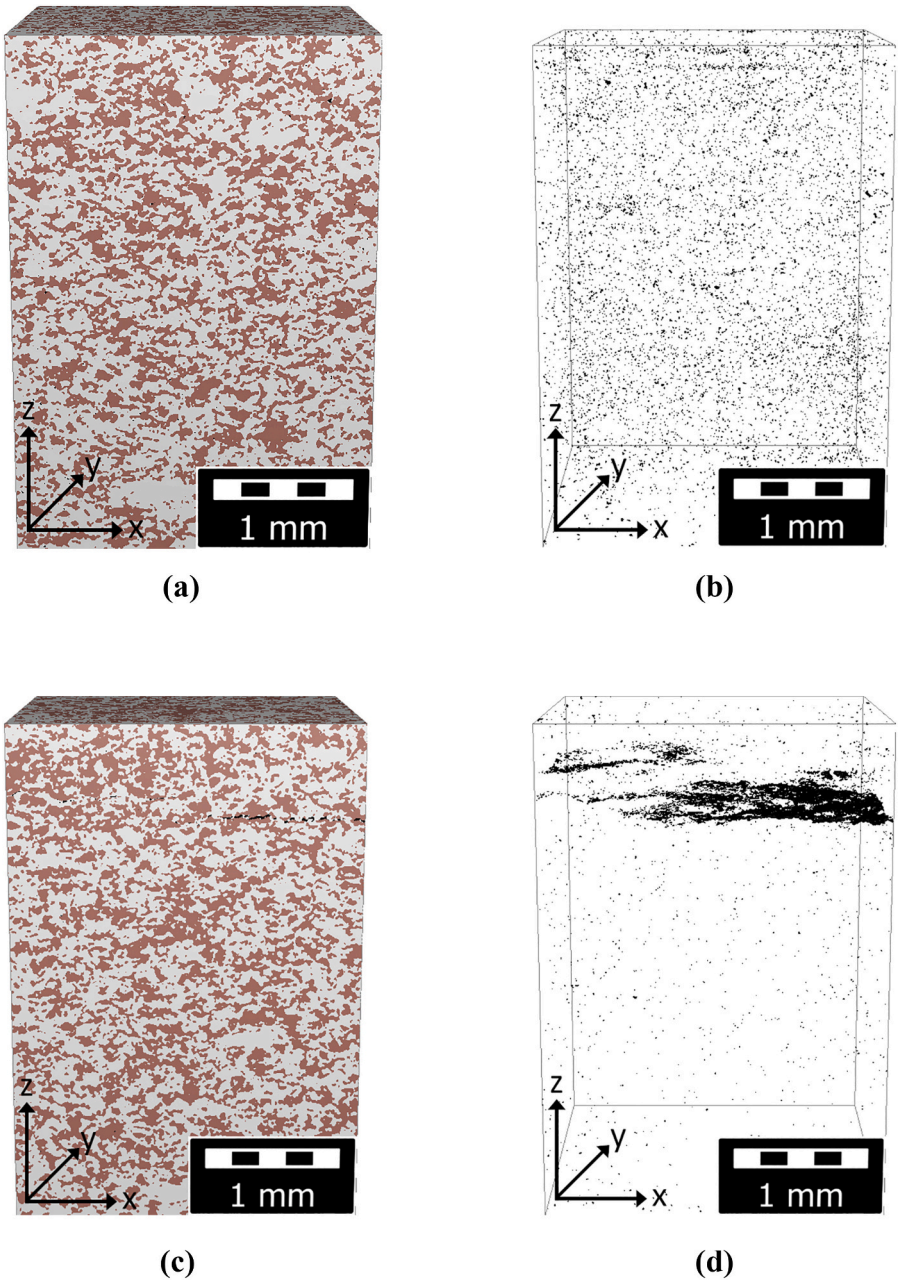

Fig. 14. Segmented images showing the microstructure of the tablet compressed at (a) 150 MPa and (c) 200 MPa and the corresponding pores at (c) 150 MPa and at (d) 200 MPa, showing a crack in lateral direction.

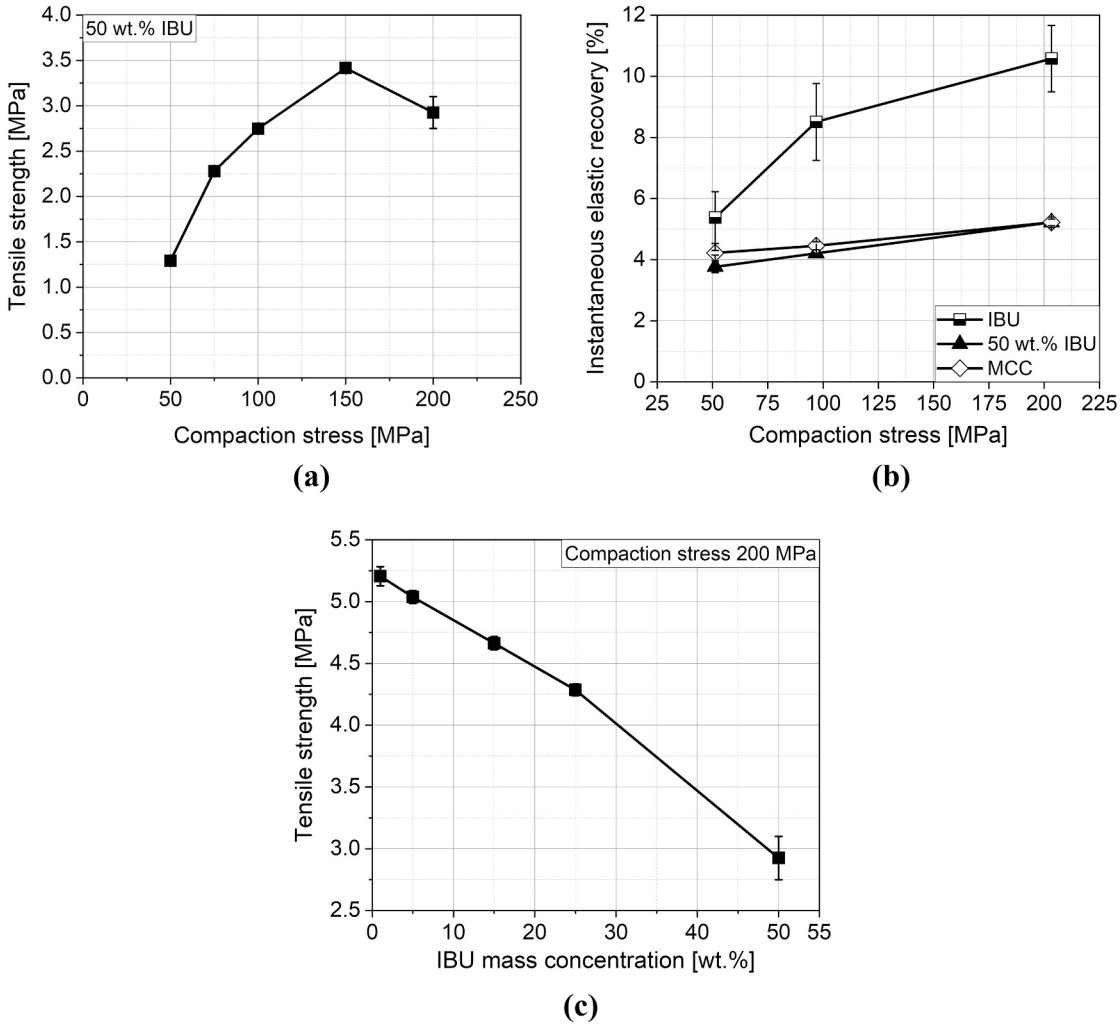

Fig. 15. Tensile strength over compaction stress for tablets with 50 wt% IBU (a), Instantaneous elastic recovery for tablets containing 100 and 50 wt% IBU as well as pure MCC (b) (Wünsch et al., 2021), tensile strength for different IBU mass concentrations (c).

In order to deeper understand the crack formation, Wu et al. applied Finite Element Method (FEM)-Simulations to identify the shear stress distribution inside the tablets. Although the shape of the tablets investigated by Wu et al. are more complex due to concave punches, local stresses in the upper part of the flat-faced tablets might contribute to the emergence of cracks.

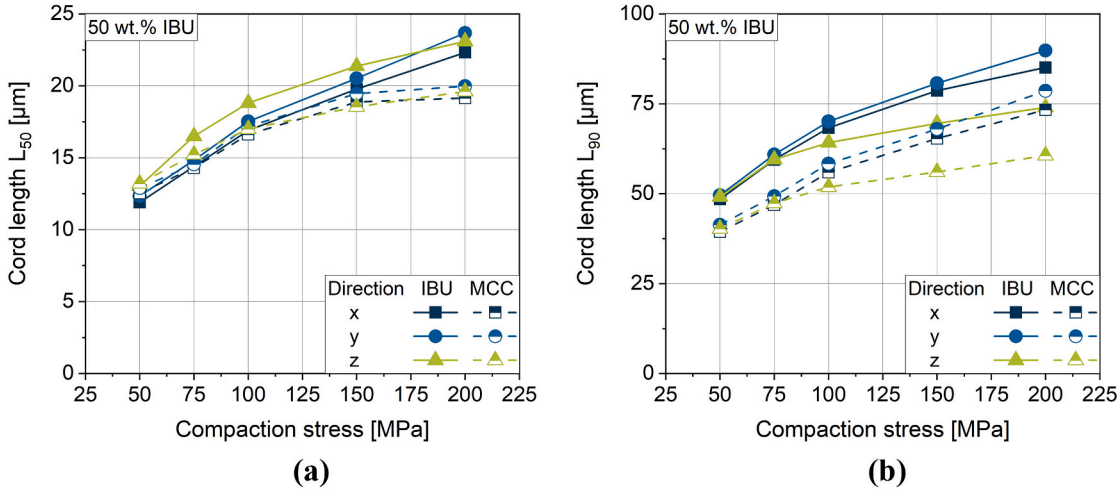

Fig. 16. Cord length of IBU and MCC in the microstructure of the tablets with increasing compaction stress: L50 (a), L90 (b).

3.6. Cord length of the solid phases – Insights into the connectivity of the microstructure

The cord length can be interpreted as a measure for the connectivity of the microstructure, as it describes how many successive voxels in one direction (x, y or z) belong to the same phase. The higher the cord length, the higher the connectivity of the respective phase in the respective direction is. The result of the cord length analysis is a distribution for each direction for the two solid phases IBU and MCC, where L_{50} and L_{90} are extracted and discussed below (Fig. 16). The L_{50} represents the median of the cord length distribution, while 90% of the cord lengths are shorter than L_{90}. These representative values result from interpolations of the discrete distribution. Besides L_{50} and L_{90}, also L_{10} was considered, at which 10% of the cord lengths are smaller than L_{10}. However, the minimal cord length of 5.06 µm already has a proportion over 10%, thus the L_{10} is an interpolation between 0 and 5.06 µm. As these values are below the resolution of the XMT, they are not displayed and discussed in the following.

Generally, the cord lengths (L_{50} approx. 12.5 µm at 50 MPa for IBU and MCC) are distinctively lower than the particle sizes measured by laser diffraction (MCC $x_{50} = 63$ µm; IBU, $x_{50} = 31$ µm). The lower cord length might result from intraparticular pores. With increasing compaction stress, the cord lengths of IBU as well as of MCC increase in general in all three directions. Therefore, the corresponding phases present growing clusters or single clusters with an increasing connectivity to others due to the compaction stress. The median value L_{50} is mostly independent of direction, whereas L_{90} presents lower values in the z-direction of compaction for both phases. This indicates a narrower cord length distribution in z-direction. Under the applied stresses, the powder volume is reduced in z-direction, leading to a rearrangement of particles and deformation of clusters preferably in the horizontal plane (x, y), resulting in a higher L_{90} in x and y direction (Fig. 16 b).A lower L_{90} in z-direction, starting to differ from those of x- and y-direction above 75 MPa, displays that the connectivity in z-direction is limited and may lead to failure perpendicular to this direction. This is in accordance with the well-known occurrence of cracks or lamination along the horizontal x-y-plane as also detected in Fig. 14 d.

In general, the L_{90} is lower for MCC than for IBU, which can be explained by the generally higher volume fraction of IBU (58.07 vol%) and the observed occurrence of clusters of IBU.

In contrast to IBU, the L_{50} of the cord length of MCC flattens for a compaction stress of 200 MPa, which is in good accordance with the declining tablets tensile strength (Fig. 15 a). The weakening of the microstructure by the crack at 200 MPa is represented here and supports the hypothesis that the strength mainly results from the connectivity of MCC.

However, it has to be considered that the cord length only presents successive voxels of the same phase, while for the connectivity of a network, and therefore its strength, connections in all directions (diagonal as well asin x, y and z direction) are important. Therefore, an analysis of the tortuosity of the solid phases may present a more appropriate method to investigate the MCC network and connect the information with the tablet strength. Additionally, the limited resolution of the XMT images has to be considered to result in wrongly segmented solid phases due to the undetected void volume. Nevertheless, the cord length analysis presents results, which are in good agreement to other observations such as the IBU clusters and the tensile strength. Thus, the cord length-method is appropriate for a first evaluation of the microstructure, provided by XMT, to determine the connectivity in combination with the tablet properties as well as the tensile strength.

4. Conclusion and outlook

In the present study, methodologies for a systematic characterization based on XMT measurements and image processing were applied to visualize and investigate the microstructure of tablets consisting of the API Ibuprofen and the excipient microcrystalline cellulose. Image segmentation of three phases (excipient, API, pores) was performed on relatively large volumes with a resolution of $(5.06\ \mu m)^3$ of the voxels. This limits the identification of small pores, which results in an underestimation (50–75%) of the porosity and an overestimation of the solid phase of the lower density. However, deviations amount to less than 5%. A higher number of larger pores (approx. 40% of pore volume > 5 µm at 100 MPa) are detected by XMT while MIP yields higher fractions of small pores ($> 95\%$ of pore volume < 5 µm at 100 MPa). FIB-SEM however confirmed the existence of both, large and small pores within the tablets. Accordingly, XMT is a useful tool for determining true internal pore sizes (instead of bottlenecks), which may in the future, better contribute to the understanding of tablet strength.

Respecting the necessary size of ROIs, the microstructure can be examined regarding the distribution and the homogeneity of the IBU. Coarse IBU clusters resulting from agglomeration in former process steps, such as blending, are visualized and can be interpreted towards their deformation based on the applied stresses and their connectivity in view of tablet strength. Such clusters resulted in high values for the empirical standard deviation, especially for low IBU contents, which may lead to varying contents between the parts of divided tablets or between different tablets in general. This inhomogeneity may lead to a high local stress gradient during the elastic recovery after compaction due to the differing instantaneous elastic recovery behavior of the pure substances. In consequence, cracks can be proved by XMT when they are inconceivable from the tablet surface. However, internal cracks (at 200 MPa compaction stress) directly coincides with a loss of tensile strength. In addition, cord length analysis was introduced to provide direction-specific information on the connectivity of each solid phase, providing anisotropy information and measuring the deformation of particles (lower cord-lengths in narrower distributions in z-direction) and stagnation or loss of connectivity at high stress (200 MPa) connected with internal cracks.

These presented methods can be used as tools to identify critical effects on the quality attributes of pharmaceutical tablets, such as on bond networks, and, by that, supply crucial information. Prior process steps, like mixing and filling procedures also influence blend properties (homogeneity and the size of particle clusters inside the blend).Therefore, the distribution and dispersion of IBU and excipient within the tablet structure as well as their impacts on mechanical properties should be analyzed by XMT measurements in more detail in future studies. Here, different aspects can be considered to obtain images of higher quality. Thus, a more precise analysis of the phase and especially pore distribution can be conducted. First, a higher resolution of the resulting image would improve the quality, although the inspected volume decreases simultaneously. Using tablets with a lower diameter might contribute to better results as the penetration depth decreases and therefore the reduction of the X-ray intensity decreases as well, leading to a better intensity resolution. An XMT device with a higher resolution of the CCD camera would further contribute to better results. Alternatively, a synchrotron, providing only monochromatic X-ray beams, enables a better differentiation between different solid densities and thus, between the different phases. Instead of standard X-ray imaging methods like computed tomography which detect differences in the intensity after transmitting through the sample, an alternative method called phase-contrast X-ray imaging or phase-sensitive X-ray imaging can be used. Here, the contrast-to-noise ratio can be improved using X-ray interferometry, which measures the X-ray deflection, providing more detailed information about density variations especially to low densities.

Using different imaging techniques, like FIB-SEM and Raman in parallel, might also be an interesting approach to gain deeper insight locally into the pore structure and the distribution of API and excipient.

Funding

This paper evolved of the research project "Simulation of distributed product structures in combined discrete and continuous production processes for solid, particulate products" which is funded by the Deutsche Forschungsgemeinschaft (DFG, German Research Foundation) – 413141366.

Declaration of Competing Interest

The authors declare that they have no known competing financial interests or personal relationships that could have appeared to influence the work reported in this paper.

Acknowledgements

The authors acknowledge and thank Novartis Pharma, Basel for the support by providing the data of the particle size distribution and the SEM-images of the powders used as well as for the provision of testing materials (IBU, MCC).

References

Akseli, I., Iyer, S., Lee, H.P., Cuitiño, A.M., 2011. A quantitative correlation of the effect of density distributions in roller-compacted ribbons on the mechanical properties of tablets using ultrasonics and X-ray tomography. AAPS PharmSciTech 12, 834–853. https://doi.org/10.1208/s12249-011-9640-z.

Akseli, I., Abebe, A., Sprockel, O., Cuitiño, A.M., 2013. Mechanistic characterization of bilayer tablet formulations. Powder Technol. 236, 30–36. https://doi.org/10.1016/j.powtec.2012.05.048.

Alderborn, G., Pasanen, K., Nyström, C., 1985. Studies on direct compression of tablets. XI. Characterization of particle fragmentation during compaction by permeametry measurements of tablets. Int. J. Pharm. 23, 79–86.

Bollmann, S., Kleinebudde, P., 2021. Evaluation of different pre-processing methods of X-ray micro computed tomography images. Powder Technol. 381, 539–550. https://doi.org/10.1016/j.powtec.2020.11.074.

Burch, S., 2002. Measurement of density variations in compacted parts using X-ray computerised tomography. Metal Powder Report 57, 24–28. https://doi.org/10.1016/S0026-0657(02)85009-3.

Busignies, V., Leclerc, B., Porion, P., Evesque, P., Couarraze, G., Tchoreloff, P., 2006. Quantitative measurements of localized density variations in cylindrical tablets using X-ray microtomography. Eur. J. Pharm. Biopharm. 64, 38–50. https://doi.org/10.1016/j.ejpb.2006.02.007.

Cabiscol, R., Finke, J.H., Zetzener, H., Kwade, A., 2018. Characterization of Mechanical Property Distributions on Tablet Surfaces. Pharmaceutics 10.

Crean, B., Parker, A., Le Roux, D., Perkins, M., Luk, S.Y., Banks, S.R., Melia, C.D., Roberts, C.J., 2010. Elucidation of the internal physical and chemical microstructure of pharmaceutical granules using X-ray micro-computed tomography, Raman microscopy and infrared spectroscopy. Eur. J. Pharm. Biopharm. 76, 498–506. https://doi.org/10.1016/j.ejpb.2010.08.006.

Fang, L., Yin, X., Wu, L., He, Y., He, Y., Qin, W., Meng, F., York, P., Xu, X., Zhang, J., 2017. Classification of microcrystalline celluloses via structures of individual particles measured by synchrotron radiation X-ray micro-computed tomography. Int. J. Pharm. 531, 658–667. https://doi.org/10.1016/j.ijpharm.2017.05.019.

Farber, L., Tardos, G., Michaels, J.N., 2003. Use of X-ray tomography to study the porosity and morphology of granules. Powder Technol. 132, 57–63. https://doi.org/10.1016/S0032-5910(03)00043-3.

Feinauer, J., Spettl, A., Manke, I., Strege, S., Kwade, A., Pott, A., Schmidt, V., 2015. Structural characterization of particle systems using spherical harmonics. Mater. Charact. 106, 123–133. https://doi.org/10.1016/j.matchar.2015.05.023.

Fell, J.T., Newton, J.M., 1970. Determination of Tablet Strength by the Diametral-Compression Test. J. Pharm. Sci. 59, 688–691. https://doi.org/10.1002/jps.2600590523.

Garner, S., Ruiz, E., Strong, J., Zavaliangos, A., 2014. Mechanisms of crack formation in die compacted powders during unloading and ejection: an experimental and modeling comparison between standard straight and tapered dies. Powder Technol. 264, 114–127. https://doi.org/10.1016/j.powtec.2014.04.086.

Gioumouxouzis, C.I., Katsamenis, O.L., Fatouros, D.G., 2020. X-ray microfocus computed tomography: a powerful tool for structural and functional characterisation of 3D printed dosage forms. J. Microsc. 277, 135–139. https://doi.org/10.1111/jmi.12798.

Hancock, B.C., Mullarney, M.P., 2005. X-ray microtomography of solid dosage forms. Pharmaceutical Technology 29 (44), 92–100.

Hiestand, E.N., Wells, J.E., Peot, C.B., Ochs, J.F., 1977. Physical processes of tableting. J. Pharm. Sci. 66, 510–519. https://doi.org/10.1002/jps.2600660413.

Inman, S.J., Briscoe, B.J., Pitt, K.G., 2007. Topographic Characterization of Cellulose Bilayered Tablets Interfaces. Chem. Eng. Res. Des. 85, 1005–1012. https://doi.org/10.1205/cherd06188.

Juppo, A.M., 1996. Relationship between breaking force and pore structure of lactose, glucose and mannitol tablets. Int. J. Pharm. 127, 95–102.

Landis, E.N., Keane, D.T., 2010. X-ray microtomography. Mater. Charact. 61, 1305–1316. https://doi.org/10.1016/j.matchar.2010.09.012.

Lannutti, J.J., 1997. Characterization and Control of Compact Microstructure. MRS Bull. 22, 38–44. https://doi.org/10.1557/S0883769400034734.

Leißner, T., Diener, A., Löwer, E., Ditscherlein, R., Krüger, K., Kwade, A., Peuker, U.A., 2020. 3D ex-situ and in-situ X-ray CT process studies in particle technology – a perspective. Adv. Powder Technol. 31, 78–86. https://doi.org/10.1016/j.apt.2019.09.038.

Leuenberger, H., Bonny, J.D., Lerk, C.F., Vromans, H., 1989. Relation between crushing strength and internal specific surface area of lactose compacts. Int. J. Pharm. 52, 91–100.

Li, H., Yin, X., Ji, J., Sun, L., Shao, Q., York, P., Xiao, T., He, Y., Zhang, J., 2012. Microstructural investigation to the controlled release kinetics of monolith osmotic pump tablets via synchrotron radiation X-ray microtomography. Int. J. Pharm. 427, 270–275. https://doi.org/10.1016/j.ijpharm.2012.02.017.

Ma, X., Kittikunakorn, N., Sorman, B., Xi, H., Chen, A., Marsh, M., Mongeau, A., Piché, N., Williams, R.O., Skomski, D., 2020. Application of deep learning convolutional neural networks for internal tablet defect detection: high accuracy, throughput, and adaptability. J. Pharm. Sci. 109, 1547–1557. https://doi.org/10.1016/j.xphs.2020.01.014.

Maire, E., Withers, P.J., 2014. Quantitative X-ray tomography. Int. Mater. Rev. 59, 1–43. https://doi.org/10.1179/1743280413Y.0000000023.

Markl, D., Wang, P., Ridgway, C., Karttunen, A.-P., Chakraborty, M., Bawuah, P., Pääkkönen, P., Gane, P., Ketolainen, J., Peiponen, K.-E., et al., 2017. Characterization of the Pore Structure of Functionalized Calcium Carbonate Tablets by Terahertz Time-Domain Spectroscopy and X-Ray Computed Microtomography. J. Pharm. Sci. 106, 1586–1595. https://doi.org/10.1016/j.xphs.2017.02.028.

Markl, D., Strobel, A., Schlossnikl, R., Bøtker, J., Bawuah, P., Ridgway, C., Rantanen, J., Rades, T., Gane, P., Peiponen, K.-E., et al., 2018. Characterisation of pore structures of pharmaceutical tablets: a review. Int. J. Pharm. 538, 188–214. https://doi.org/10.1016/j.ijpharm.2018.01.017.

Mazel, V., Diarra, H., Malvestio, J., Tchoreloff, P., 2018. Lamination of biconvex tablets: Numerical and experimental study. Int. J. Pharm. 542, 66–71. https://doi.org/10.1016/j.ijpharm.2018.03.012.

Miguélez-Morán, A.M., Wu, C.-Y., Dong, H., Seville, J.P.K., 2009. Characterisation of density distributions in roller-compacted ribbons using micro-indentation and X-ray micro-computed tomography. Eur. J. Pharm. Biopharm. 72, 173–182. https://doi.org/10.1016/j.ejpb.2008.12.005.

Neumann, M., Cabiscol, R., Osenberg, M., Markötter, H., Manke, I., Finke, J.H., Schmidt, V., 2019. Characterization of the 3D microstructure of Ibuprofen tablets by means of synchrotron tomography. J. Microsc. 274, 102–113. https://doi.org/10.1111/jmi.12789.

Nordström, J., Persson, A.-S., Lazorova, L., Frenning, G., Alderborn, G., 2013. The degree of compression of spherical granular solids controls the evolution of microstructure and bond probability during compaction. Int. J. Pharm. 442, 3–12. https://doi.org/10.1016/j.ijpharm.2012.08.011.

Otsu, N., 1979. A Threshold selection Method from Gray-Level Histograms. IEEE Transactions on Systems, Man, and Cybernetics 9, 62–66.

Rigby, S.P., van der Walle, C.F., Raistrick, J.H., 2004. Determining drug spatial distribution within controlled delivery tablets using MFX imaging. J. Control. Release 96, 97–100. https://doi.org/10.1016/j.jconrel.2004.01.007.

Schüth, F., 2002. Handbook of Porous Solids. Wiley-VCH, Weinheim (ISBN 9783527302468).

Sinka, I.C., Burch, S.F., Tweed, J.H., Cunningham, J.C., 2004. Measurement of density variations in tablets using X-ray computed tomography. Int. J. Pharm. 271, 215–224. https://doi.org/10.1016/j.ijpharm.2003.11.022.

Strege, S., Weuster, A., Zetzener, H., Brendel, L., Kwade, A., Wolf, D.E., 2014. Approach to structural anisotropy in compacted cohesive powder. Granul. Matter 16, 401–409. https://doi.org/10.1007/s10035-013-0454-4.

Sun, C.C., 2017. Microstructure of Tablet-Pharmaceutical significance, Assessment, and Engineering. Pharm. Res. 34, 918–928. https://doi.org/10.1007/s11095-016-1989-y.

Sun, W.-J., Rantanen, J., Sun, C.C., 2018. Ribbon density and milling parameters that determine fines fraction in a dry granulation. Powder Technol. 338, 162–167. https://doi.org/10.1016/j.powtec.2018.07.009.

Torquato, S., Lu, B., 1993. Chord-length distribution function for two-phase random media. Phys. Rev. E 47, 2950–2953.

Venables, H.J., Wells, J.I., 2001. Powder mixing. Drug Dev. Ind. Pharm. 27, 599–612. https://doi.org/10.1081/DDC-100107316.

Wagner-Hattler, L., Québatte, G., Keiser, J., Schoelkopf, J., Schlepütz, C.M., Huwyler, J., Puchkov, M., 2020. Study of drug particle distributions within mini-tablets using synchrotron X-ray microtomography and superpixel image clustering. Int. J. Pharm. 573, 118827. https://doi.org/10.1016/j.ijpharm.2019.118827.

Washburn, E.W., 1921. Note on a Method of determining the distribution of Pore Sizes in a porous Material. Physics 7.

Wiedey, R., Kleinebudde, P., 2017. The Density distribution in Ribbons from Roll Compaction. Chemie Ingenieur Technik 89, 1017–1024.

Wray, P., Chan, K.L.A., Kimber, J., Kazarian, S.G., 2008. Compaction of pharmaceutical tablets with different polymer matrices studied by FTIR imaging and X-ray microtomography. J. Pharm. Sci. 97, 4269–4277. https://doi.org/10.1002/jps.21309.

Wu, C.-Y., Ruddy, O.M., Bentham, A.C., Hancock, B.C., Best, S.M., Elliott, J.A., 2005. Modelling the mechanical behaviour of pharmaceutical powders during compaction. Powder Technol. 152, 107–117. https://doi.org/10.1016/j.powtec.2005.01.010.

Wu, C.Y., Bentham, A.C., Mills, A., 2007. Analysis of failure mechanisms during powder compaction. MSF 534-536, 237–240. https://doi.org/10.4028/www.scientific.net/MSF.534-536.237.

Wu, C.-Y., Hancock, B.C., Mills, A., Bentham, A.C., Best, S.M., Elliott, J.A., 2008. Numerical and experimental investigation of capping mechanisms during pharmaceutical tablet compaction. Powder Technol. 181, 121–129. https://doi.org/10.1016/j.powtec.2006.12.017.

Wünsch, I., Finke, J.H., John, E., Juhnke, M., Kwade, A., 2021. The influence of particle size on the application of compression and compaction models for tableting. Int. J. Pharm. 599, 120424. https://doi.org/10.1016/j.ijpharm.2021.120424.

Yost, E., Chalus, P., Zhang, S., Peter, S., Narang, A.S., 2019. Quantitative X-Ray Microcomputed Tomography Assessment of Internal Tablet Defects. J. Pharm. Sci. 108, 1818–1830. https://doi.org/10.1016/j.xphs.2018.12.024.